

Article

Theoretical Study of As₂O₃ Adsorption Mechanisms on CaO surface

Yaming Fan ^{1,2,†}, Qiyu Weng ^{2,3,4,†}, Yuqun Zhuo ^{2,3,4,*}, Songtao Dong ¹, Pengbo Hu ^{2,3,4} and Duanle Li ^{2,3,4} 

¹ Research Institute of Petroleum Processing, SINOPEC, Beijing 100083, China; fanymthu@163.com (Y.F.); dongst.ripp@sinopec.com (S.D.)

² Key Laboratory for Thermal Science and Power Engineering of the Ministry of Education, Department of Energy and Power Engineering, Tsinghua University, Beijing 100084, China; wqy17@mails.tsinghua.edu.cn (Q.W.); hupb18@mails.tsinghua.edu.cn (P.H.); liduanle@163.com (D.L.)

³ Tsinghua University-University of Waterloo Joint Research Center for Micro/Nano Energy and Environment Technology, Tsinghua University, Beijing 100084, China

⁴ Beijing Engineering Research Center for Ecological Restoration and Carbon Fixation of Saline-alkaline and Desert Land, Tsinghua University, Beijing 100084, China

* Correspondence: zhuoyq@mail.tsinghua.edu.cn

† These authors contributed equally to this work.

Received: 23 January 2019; Accepted: 18 February 2019; Published: 25 February 2019



Abstract: Emission of hazardous trace elements, especially arsenic from fossil fuel combustion, have become a major concern. Under an oxidizing atmosphere, most of the arsenic converts to gaseous As₂O₃. CaO has been proven effective in capturing As₂O₃. In this study, the mechanisms of As₂O₃ adsorption on CaO surface under O₂ atmosphere were investigated by density functional theory (DFT) calculation. Stable physisorption and chemisorption structures and related reaction paths are determined; arsenite (AsO₃³⁻) is proven to be the form of adsorption products. Under the O₂ atmosphere, the adsorption product is arsenate (AsO₄³⁻), while tricalcium orthoarsenate (Ca₃As₂O₈) and dicalcium pyroarsenate (Ca₂As₂O₇) are formed according to different adsorption structures.

Keywords: CaO; As₂O₃; DFT; adsorption

1. Introduction

Arsenic is a hazardous element existing in fossil fuels such as coal and petroleum [1]. According to the properties of arsenic and its compounds, it has been classified as volatile trace element by Clark and Sloss [2]. During combustion or chemical industry processes, gaseous arsenic is released into the environment. Excess amounts of arsenic can pollute water and soil. The exposure of arsenic to human may lead to hyperpigmentation, keratosis, skin and lung cancers with high possibility [3,4]. Arsenic compounds (including inorganic arsine) have been identified as hazardous air pollutants by the US government since 1990 [5]. The concentration of atmospheric arsenic in China is 51.0 ng/m³, which is much higher than the limit of NAAQS (6.0 ng/m³, GB 3095-2012) and the limit of WHO (6.6 ng/m³, WHO) [6].

Combustion of fossil fuels, especially coal, is one of the main sources for anthropogenic emission of atmospheric arsenic [7]. It was estimated that 335.5 tons of atmospheric arsenic were emitted from Chinese coal-fired plants in 2010 [8]. In 2011, the US Environmental Protection Agency issued the Mercury and Air Toxics Standards (US, MATS, updated in 2016). An arsenic emission limit of 3.0×10^{-3} lb/MWh (approximately 0.41 μg/m³) was set for coal-fired power plants [9]. In Chinese coal-fired power plants, the control of arsenic still remains scarce, but there are increasing interests in understanding its transformation in flue gas and developing emission reduction techniques.

Under an oxidizing atmosphere, gaseous As_2O_3 should be the main form of arsenic combustion products [10]. It has been proven that CaO could adsorb As_2O_3 in the coal-fired flue gas, and the dominating products were arsenate (AsO_4^{3-}) [11–14]. CaO component in fly ash leads to the enrichment of arsenic [15–18]. R.O. Sterling [11] found that CaO could effectively adsorb As_2O_3 at 600 °C and 1000 °C; the adsorption products were $\text{Ca}_3\text{As}_2\text{O}_8$ when O_2 existed. Jadhav [12] studied the adsorption products of As_2O_3 on a CaO surface under O_2 atmosphere between 300 °C and 1000 °C. X-ray photoelectron spectroscopy (XPS) and X-ray Diffraction (XRD) reflected that, when temperature was lower than 600 °C, the adsorption product was $\text{Ca}_3\text{As}_2\text{O}_8$; when temperature was between 700 °C and 900 °C, the adsorption products was $\text{Ca}_2\text{As}_2\text{O}_7$; and when temperature was as high as 1000 °C, the adsorption product was $\text{Ca}_3\text{As}_2\text{O}_8$. He also revealed that SO_2 and HCl played a weak role in adsorption. Li [13,14] studied the influence of CO_2 and SO_2 on the capture of As_2O_3 by CaO. The existence of SO_2 and CO_2 did not change the form of arsenic in adsorption products. The previous study certified the strong adsorption of As_2O_3 on CaO surface and the important role O_2 played in the reaction. However, the acute toxicity and low concentration of arsenic significantly limit the experimental research of As_2O_3 adsorption. The adsorption mechanisms still remain unclear, especially the composition of adsorption active sites and product structures.

Quantum chemistry calculation based on density functional theory (DFT) has become an effective method to simulate structures [19] and surface reaction of volatile trace elements [20]. For example, the adsorption of As^0 on a CaO (001) surface has been effectively studied by Zhang [21]. In this study, the adsorption structures and the detailed adsorption steps between the CaO surface and As_2O_3 (under O_2 atmosphere) have been studied by advanced DFT calculation, with the aim to offer microscopic information about critical reactions, and thus, to provide guidance to develop more efficient adsorbents and related control technologies.

2. Methods and Modeling

2.1. Methods

The material studio CASTEP [22,23] module was applied in the DFT calculation. The GGA (Generalized Gradient Approximation) and PBE [24] (Perdew-Burke-Ernzerhof) were chosen to describe the exchange and correlation interactions. The electronic wave functions were expanded on a plane wave basis with cut-off energy of 380 eV. The ultra-soft pseudo potential was referred to describe the interactions between electrons and the ionic cores [25]. ‘The spin-polarized’ option was selected for ‘spin-unrestricted’ calculations [26]. The BFGS (Broyden-Fletcher-Goldfarb-Shanno) optimization algorithm was chosen for geometry optimization [27]. The transition state and reaction path (intermediate states) was determined by using the complete Linear Synchronous Transit/Quadratic Synchronous Transit (LST/QST) method [28] and confirmed by the Nudged-Elastic Band (NEB) method [29].

The convergence criteria of geometry optimization included: (a) self-consistent field (SCF) of 5.0×10^{-7} eV/atom; (b) energy of 5×10^{-6} eV/atom; (c) displacement of 5×10^{-4} Å; (d) force of 0.01 eV/Å; and (e) stress of 0.02 GPa. The convergence of complete LST/QST method (RMS, Root Mean Square) was set to 0.05 eV/Å. The convergence criteria of NEB included: (a) energy of 1.0×10^{-5} eV/atom; (b) max force of 0.05 eV/Å; and (c) max displacement of 0.004 Å.

The adsorption energy (E_{ads}) was defined as follows:

$$E_{ads} = E_{pro} - (E_{slab} + E_{adsorbate}) \quad (1)$$

where E_{pro} was the total energy of adsorption product, E_{slab} was the total energy of the slab model, and $E_{adsorbate}$ was the total energy of isolated adsorbate As_2O_3 or O_2 at its equilibrium geometry. A negative E_{ads} value represented a stable adsorption system.

2.2. Modeling

The energy of CaO crystal cell was converged with $6 \times 6 \times 6$ k points in the Monkhorst-pack grid [30]. The equilibrium geometry of As_2O_3 and O_2 was examined in a cell of $20 \times 20 \times 20 \text{ \AA}^3$ periodic box. As shown in Table 1, the values of the calculated bond lengths, angles, and lattice parameters are consistent with the data reported from the previous study, indicating the reliability of the calculation.

Table 1. Calculated lattice parameters, bond lengths, and bond angles.

Substance	Previous Data	Simulated Data
CaO [31,32]	4.836 Å/4.807 Å	4.837 Å
As_2O_3 [33]	As–O bond 1.794 Å	As–O bond 1.814 Å
	As–O bond 1.610 Å	As–O bond 1.622 Å
	O–As–O angle 106.3°	O–As–O angle 111.2°
	As–O–As angle 133.8°	As–O–As angle 141.8°
O_2 [34]	O–O 1.210 Å	O–O 1.240 Å

In our previous study, the CaO(001) slab model has been widely used for CO_2 [35], Se^0 [36] and SeO_2 [37] heterogeneous adsorption reaction, in which the good consistency with experimental work has been proven. Similarly, a 4-layer 3×3 -surface CaO (001) slab was modeled to describe the CaO surface between CaO and As_2O_3 in this study. The superficial two layers of atoms were relaxed while the rest layers were fixed [38]. The vacuum region between slabs was set to 10 Å to avoid interactions among periodic images [39]. The energy of slab models and related adsorption structures were converged with $2 \times 2 \times 1$ k points in the Monkhorst-pack grid. The detailed modeling process was put in the Supplementary Materials (Optimization of slab model section: Tables S1 and S2).

3. Results and Discussions

According to the spatial position of As_2O_3 and surface atoms distribution, three groups, including twenty-one possible As_2O_3 structures, were first modeled as the initial structures for optimization (provided in Figure S1). After the geometric optimization of the initial structures, plenty of adsorption structures were validated, then the possible reaction paths were calculated. Based on the minimal point of the reaction paths, additional stable structures were acquired. Most of the physisorption structures were similar in terms of structural pattern and close in terms of energy level; thus, three representative physisorption structures (adsorption energy higher than -100 kJ/mol [40]) were determined. Additionally, ten chemisorption structures (adsorption energy lower than -100 kJ/mol [40]) were identified. Based on these structures, various adsorption paths were finally confirmed. For brevity, the n^{th} physisorption structure was abbreviated as P_n , while the n^{th} chemisorption structure was abbreviated as C_n .

3.1. Stable Sorption Structures

3.1.1. Stable Physisorption Structures

Three representative physisorption structures have been shown in Table 2. The dominating differences are the number of As_2O_3 's O bonded with superficial Ca and the distribution of the superficial Ca occupied by As_2O_3 's O. Three types of physisorption follow the crystal orientation $\langle 100 \rangle$, $\langle 110 \rangle$ and $\langle 110 \rangle$, respectively. Two or three superficial Ca is close to As_2O_3 's O, and the bond length is about 2.380 Å to 2.876 Å. The corresponding adsorption energy ranges from -65.8 kJ/mol to -58.4 kJ/mol. Based on electron density cloud, physisorption active sites are composed of superficial Ca atoms that interact with O of As_2O_3 .

Table 2. Stable physisorption structures, adsorption energy, electron density cloud, and E_{ads} .

Name	Top View	Front View	Electron Density Cloud	Structure Details	E_{ads}
P ₁				Bond ₁₂ : 2.450 Å Bond ₃₄ : 2.469 Å	−65.8 kJ/mol
P ₂				Bond ₁₂ : 2.380 Å	−62.6 kJ/mol
P ₃				Bond ₁₂ : 2.876 Å Bond ₃₄ : 2.539 Å	−58.4 kJ/mol

3.1.2. Stable Chemisorption Structures

Ten chemisorption structures were obtained, with E_{ads} ranging from −198.5 kJ/mol to −391.4 kJ/mol, which implies strong chemisorption. Superficial Ca is close to As_2O_3 's O, the bond length is about 2.269 Å to 2.528 Å, while superficial O is close to As_2O_3 's O, the bond length is 1.788 Å to 2.086 Å. According to electron density cloud and bond length, chemisorption active sites are superficial O atoms that interact with As of As_2O_3 . According to the adsorption energy and structure (i.e., the positions of As and O), four categories were classified in Table 3:

Category I: As_2O_3 's As is located on the hollow site

Category II: All of As_2O_3 's O is located on or close to superficial Ca top site

Category III: As_2O_3 transforms into a spoon-shaped structure

Category IV: All of As_2O_3 's As is located on two neighboring superficial O top site

Table 3. Chemisorption structures, adsorption energy, electron density cloud and E_{ads} .

Category	Name	Top View	Front View	Electron Density Cloud	Structure Details	E_{ads}
I	C ₁				Bond ₁₂ : 2.635 Å Bond ₁₄ : 2.086 Å Bond ₃₅ : 2.360 Å	−198.5 kJ/mol
II	C ₂				Bond ₁₂ : 1.858 Å Bond ₃₄ : 2.360 Å Bond ₅₆ : 2.386 Å	−222.1 kJ/mol
II	C ₃				Bond ₁₂ : 2.424 Å Bond ₃₄ : 1.815 Å Bond ₅₆ : 2.314 Å Bond ₇₈ : 2.490 Å	−274.4 kJ/mol

Table 3. Cont.

Category	Name	Top View	Front View	Electron Density Cloud	Structure Details	E_{ads}
II	C ₄				Bond ₁₂ : 2.269 Å Bond ₃₄ : 1.949 Å Bond ₅₆ : 2.391 Å	−292.0 kJ/mol
II	C ₅				Bond ₁₂ : 2.293 Å Bond ₃₄ : 1.943 Å Bond ₅₆ : 2.298 Å	−315.1 kJ/mol
III	C ₆				Bond ₁₂ : 1.815 Å Bond ₃₄ : 2.355 Å	−302.3 kJ/mol
III	C ₇				Bond ₁₂ : 1.788 Å Bond ₃₄ : 2.528 Å Bond ₅₆ : 2.514 Å Bond ₇₈ : 2.422 Å	−314.0 kJ/mol
IV	C ₈				Bond ₁₂ : 2.357 Å Bond ₃₄ : 1.901 Å Bond ₅₆ : 2.298 Å	−381.7 kJ/mol
IV	C ₉				Bond ₁₂ : 2.472 Å Bond ₃₄ : 1.869 Å Bond ₅₆ : 2.503 Å	−388.6 kJ/mol
IV	C ₁₀				Bond ₁₂ : 2.382 Å Bond ₃₄ : 1.894 Å Bond ₅₆ : 2.299 Å Bond ₇₈ : 2.392 Å	−391.4 kJ/mol

3.2. Adsorption Process

Due to the continuity of energy, the adsorption process can be characterized as an energy-drop process, including both physisorption and chemisorption.

3.2.1. Transformation Process of Physisorption Structures to Chemisorption Structures

In the following part, the transition state number n is abbreviated as TS_n , and the intermediate position number n is abbreviated as IP_n , for short.

As shown in Figure 1, when As_2O_3 approaches the surface with vibration along the surface, the physisorption structure transforms into a chemisorption structure during one or two transition state. For instance, P_1 to C_7 (Figure 1a), P_2 to C_8 (Figure 1b) and P_3 to C_8 (Figure 1c). The energy barrier is low, from 1.4 kJ/mol to 13.9 kJ/mol, suggesting that the physisorbed As_2O_3 is not stable enough and could be easily transformed into chemisorption structures by thermal vibration.

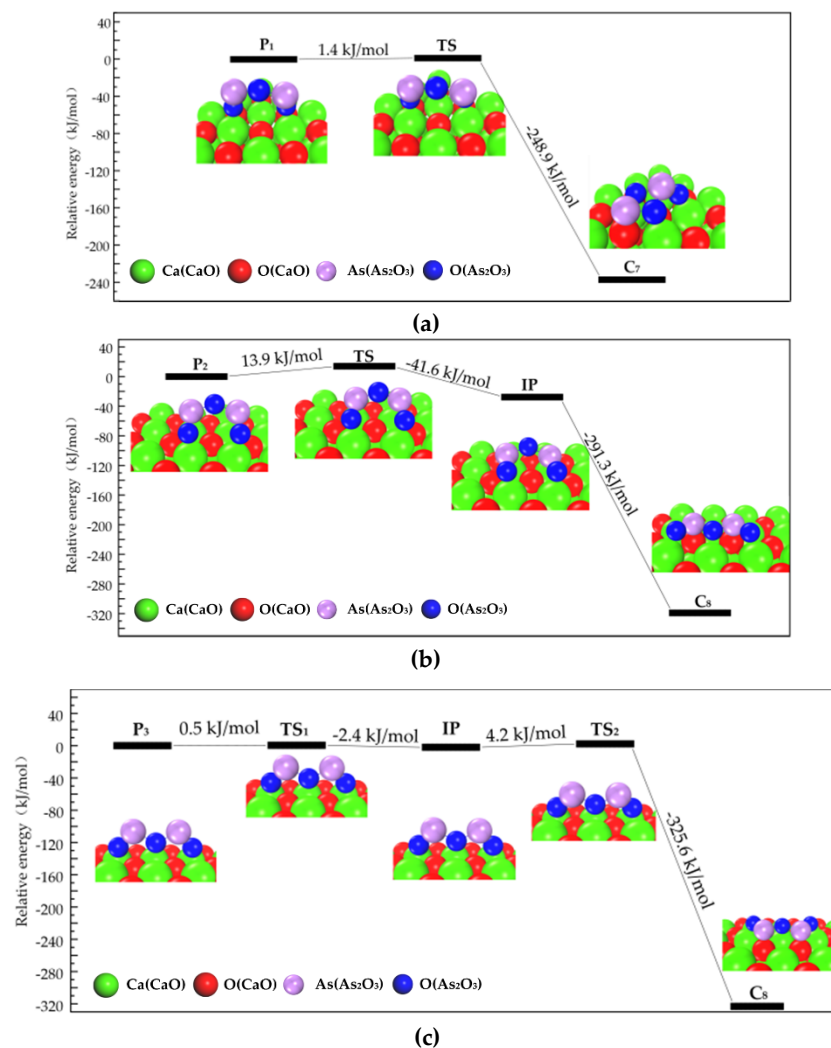


Figure 1. Structures and energies during transformation process of physisorption structures to chemisorption structures. (a) Reaction path of physisorption structure 1; (b) Reaction path of physisorption structure 2; (c) Reaction path of physisorption structure 3.

3.2.2. Transformation Process of Chemisorption Structures

Chemisorbed As_2O_3 gradually transforms into more stable structures. Different possible reaction paths were calculated. The four categories of chemisorption structures can be sorted by the E_{ads} of each as Category IV < Category III \approx Category II < Category I.

Category I has relatively high energy, i.e., relatively low stability, its transformation to Category II, III and IV could be triggered by molecular thermal vibration.

The pathway that Category I transforms to Category II is shown in Figure 2. Firstly, C_1 transforms into C_6 (Category II) and then C_5 (Category III), with the energy barrier of 10.8 kJ/mol, 16.7 kJ/mol, and 6.7 kJ/mol, respectively. As shown in Figure 2, Category I transforms into Category IV along with another reaction path, the related energy barrier is 7.4 kJ/mol. The relatively low energy barrier suggests that Category I is not stable enough, and could easily transform to Category II, III and IV.

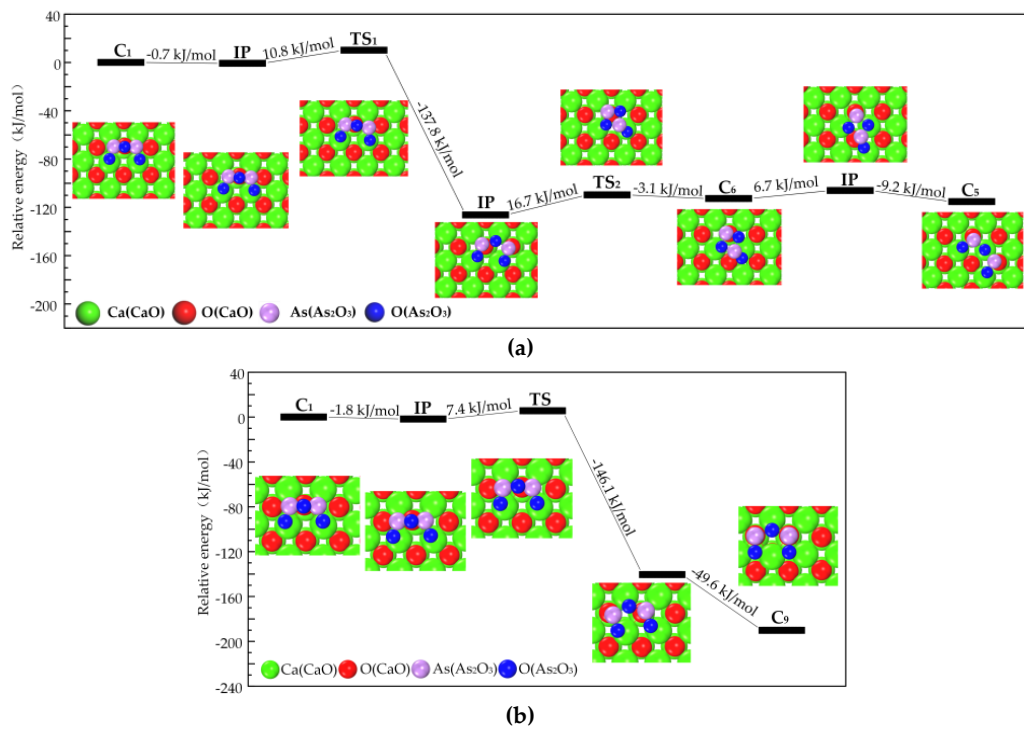


Figure 2. Transformation path of Category I. (a) Category I to Category II and III; (b) Category I to Category IV.

The reaction path of Category II is shown in Figure 3. C₃ firstly transforms into intermediate and then converts to C₉. The corresponding energy barrier is 16.1 kJ/mol and 83.0 kJ/mol, proving that Category II transforms to Category IV with the special direction of thermal vibration.

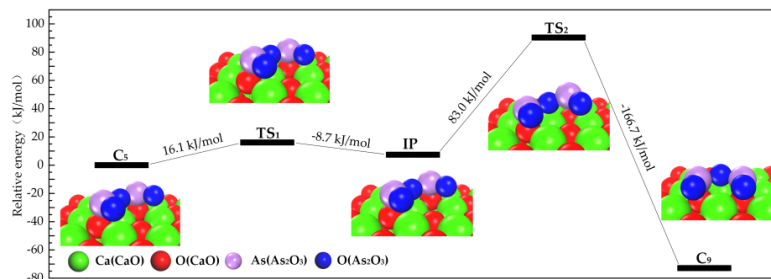


Figure 3. Transformation path of Category II.

Structures of Category III can transform into Category II, as shown in Figure 4. The spoon-shaped structure of As₂O₃ in C₇ disappears and then overcomes a 48.3 kJ/mol energy barrier to transform to C₅, indicating the conversion of Category III to Category II.

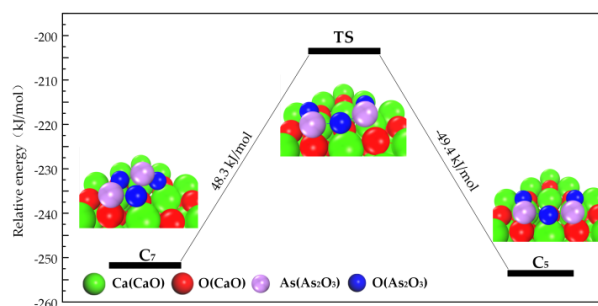


Figure 4. Transformation path of Category III.

Category IV is the most stable category. C_8 , C_9 , and C_{10} can transform into each other (shown in Figure 5). As_2O_3 's As does not move during the transformation. When all of As_2O_3 's O in C_8 vibrate, C_8 converts to C_9 , and the energy barrier is 41.6 kJ/mol (Figure 5a). When one of As_2O_3 's O in C_8 vibrates, C_8 converts to C_{10} , and the energy barrier is 153.3 kJ/mol (Figure 5b). When one of the oxygen atoms of As_2O_3 in C_9 vibrates, C_9 converts to C_{10} , and the energy barrier is 154.4 kJ/mol (Figure 5c). The difference in energy barrier is caused by the movement distance of As_2O_3 's O being motivated by thermal vibration. In the first reaction, the movement distance of As_2O_3 's O is shorter than that in the second and third reactions, which demands relatively lower energy to overcome the energy barrier.

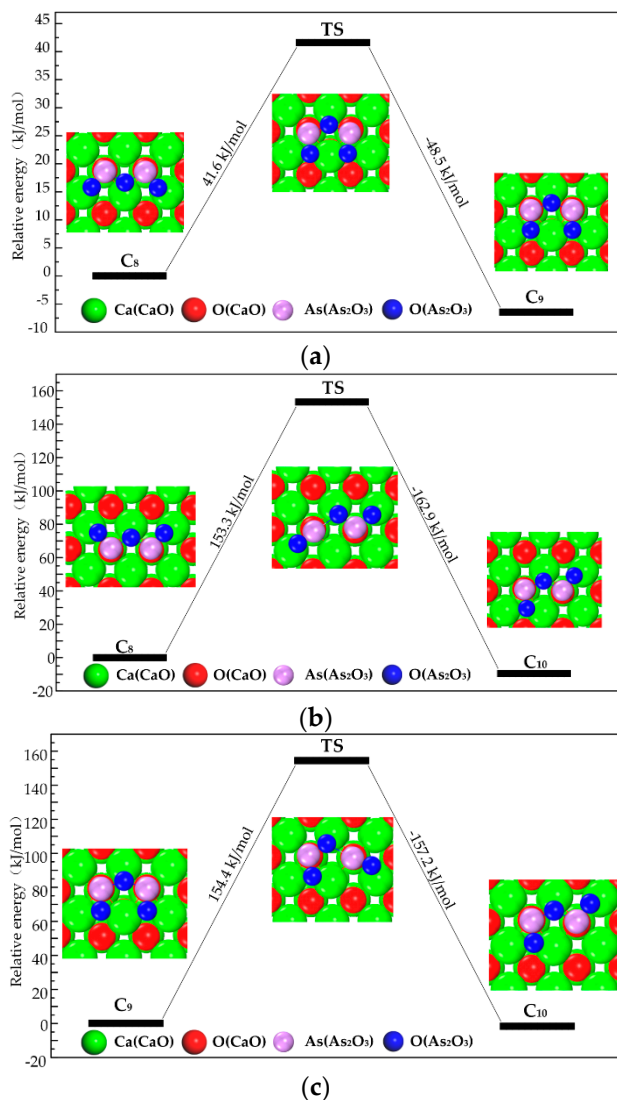


Figure 5. Transformation path of Category IV. (a) Reaction path of C_8 to C_9 ; (b) Reaction path of C_8 to C_{10} ; (c) Reaction path of C_9 to C_{10} .

3.3. Path of the Reaction

According to above-mentioned processes, the reaction paths can be concluded as follows; firstly, the isolated As_2O_3 is physisorbed on a CaO surface (As_2O_3 's O weakly interacts with superficial Ca); secondly, the physisorbed As_2O_3 transforms to chemisorbed As_2O_3 . (As_2O_3 's As interacts with superficial O); and thirdly, due to thermal vibration, the chemisorbed As_2O_3 transforms into more stable chemisorbed As_2O_3 (the position of As_2O_3 's O changed).

The adsorption path of As_2O_3 was summarized as the process shown in Figure 6. These reactions could be classified as three types according to the energy barrier with the aim to reflect the intensity of the required reaction temperature. The number of superficial CaO occupied by As_2O_3 is also considered in order to describe the adsorption reaction equation.

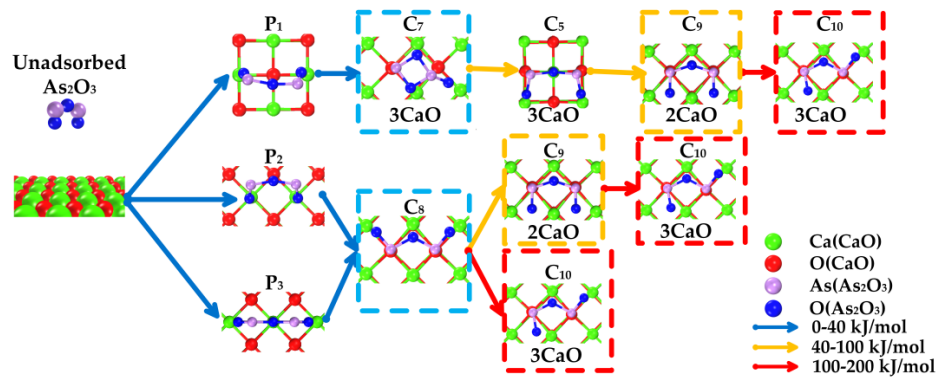


Figure 6. Overall adsorption paths of As_2O_3 on CaO.

Blue arrow: energy barrier is in the range of 0–40 kJ/mol, suggesting that reaction is likely to occur under a relatively low-temperature condition.

Yellow arrow: energy barrier is in the range of 40–100 kJ/mol, suggesting that reaction is likely to occur under a relatively medium-temperature condition.

Red arrow: energy barrier is in the range of 100–200 kJ/mol, suggesting that reaction is likely to occur under a relatively high-temperature condition.

Figure 6 reveals that three main reaction paths may exist:

1. $\text{As}_2\text{O}_3 \rightarrow \text{P}_1 \rightarrow \text{C}_7 \rightarrow \text{C}_9 \rightarrow \text{C}_{10}$;
2. $\text{As}_2\text{O}_3 \rightarrow \text{P}_2 \text{ or } \text{P}_3 \rightarrow \text{C}_8 \rightarrow \text{C}_9 \rightarrow \text{C}_{10}$;
3. $\text{As}_2\text{O}_3 \rightarrow \text{P}_2 \text{ or } \text{P}_3 \rightarrow \text{C}_8 \rightarrow \text{C}_{10}$.

Under a relatively low-temperature condition (blue arrow, 0–40 kJ/mol), the main products are C_7 and C_8 (blue grid). Three superficial Ca and one or two superficial O are involved in the reaction, representing three CaO participates in the adsorption. The adsorption equation could be written as:



Under a relatively medium-temperature condition (yellow arrow, 40–100 kJ/mol), the main products are C_9 . Two superficial Ca and two superficial O participate in the structure. The adsorption equation could be written as:



Under a relatively high-temperature condition (red arrow, 100–200 kJ/mol), the main product is C_{10} . Three superficial Ca and two superficial O are involved in the reaction (hollow Ca represents 1/2 Ca atom). The adsorption equation could be written as:



With the reaction temperature increases, adsorption product changes from $\text{Ca}_3\text{As}_2\text{O}_6$ to $\text{Ca}_2\text{As}_2\text{O}_5$ and back to $\text{Ca}_3\text{As}_2\text{O}_6$ again. Different microcosmic adsorption structures lead to different macroscopic products and reaction equation.

Besides, as shown in Figure S2, the paths of C_1 transforming to other structures have been also been found. However, no possible paths which isolated or physisorbed As_2O_3 transforms to C_1 has been found, implying C_1 is unstable or nonexistent.

3.4. Partial Density of States (PDOS)

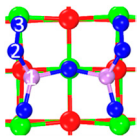
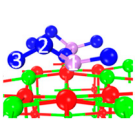
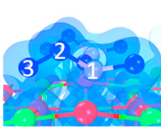
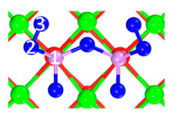
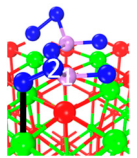
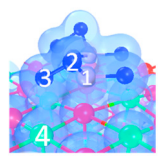
The change PDOS of As₂O₃ and CaO was put in the Supplementary Materials (Figure S3). For As₂O₃, the PDOS of physisorption structure 1, 2, and 3 are similar to each other. As the physisorption structure transforms to C₇, the *p* state orbitals near Fermi level (from −0.6 eV to 1.9 eV) drift to lower energy level, meanwhile get energy splitting and orbital reorganization, caused by the changing of As₂O₃ structure and the combination between As₂O₃'s As and superficial O. When C₇ transforms to C₅, *s* state orbital (−17.2 eV) energy level splits into two peaks of −18.0 eV and −16.9 eV, which is caused by the As-O bond breaking and the bonding between As and superficial O. When C₅ transform to C₈, the *p* state orbital (3.7 eV) and *s* state orbital (−17.9 eV) energy level both split slightly. This is the result of the slight change in the surface distribution of As₂O₃. As the adsorption products have close energies and structures, PDOS of C₉ and C₁₀ are basically similar to C₈.

For CaO slab surface, when an As₂O₃ molecule is physisorbed on the surface, little change of PDOS is detected. When As₂O₃ is chemisorbed, it can be seen that the superficial *p* orbitals around Fermi level (from −2.7 eV to 0.4 eV) drift to a lower energy range (from −5.8 eV to 0.2 eV). Moreover, a small peak (−16.8 eV) is separated from *s* orbitals (peak at −14.6 eV), proving that *s* orbitals participate in the chemisorption to some extent. Superficial *p* state orbitals near Fermi level play an important role in the chemisorption of As₂O₃. It suggests that the CaO surface's property of capturing As₂O₃ might be improved by increasing the quantities of superficial *p* orbitals near Fermi level.

3.5. Influence of O₂ on Adsorbed As₂O₃

Under the flue gas atmosphere, especially O₂-containing atmosphere, O₂ reacts with chemisorbed As₂O₃; i.e., arsenite (AsO₃^{3−}) is oxidized to arsenate (AsO₄^{3−}). As an example, two stable chemisorption structures (C₅, C₉) identified previously were presented in Table 4. The distance between As₂O₃'s As and O₂'s O is 1.763–1.764 Å, which is close to the As-O bond length of As₂O₃ (1.628 Å). The distance between O₂'s O and superficial Ca is 2.247–2.263 Å. According to the electron density cloud, one of O₂'s O overlaps with As₂O₃'s As. The other O of O₂ overlaps slightly with the superficial Ca.

Table 4. Stable chemisorption structures under O₂ atmosphere, adsorption energy, electron density cloud and E_{ads} .

Name	Top View	Front View	Electron Density Cloud	Structure Details	E_{ads}
C ₅ under O ₂				Bond ₁₂ : 1.764 Å Bond ₃₄ : 1.452 Å Bond ₅₆ : 2.263 Å	−165.2 kJ/mol
C ₈ under O ₂				Bond ₁₂ : 1.763 Å Bond ₃₄ : 1.599 Å Bond ₅₆ : 2.427 Å	−174.4 kJ/mol



Based on Figure 6 and Table 4, the reaction equation of adsorption under O₂ atmosphere can be written as Equations (5)–(7), corresponding to low-temperature, medium-temperature, and high-temperature adsorption, respectively.





With the increase of reaction temperature, adsorption product changed from $\text{Ca}_3\text{As}_2\text{O}_8$ to $\text{Ca}_2\text{As}_2\text{O}_7$ and then to $\text{Ca}_3\text{As}_2\text{O}_8$ in an O_2 -containing atmosphere. According to this research, the product under low-temperature and high-temperature conditions is $\text{Ca}_3\text{As}_2\text{O}_8$ with different structures, i.e., crystalline form. Under a medium-temperature condition, the main product is $\text{Ca}_3\text{As}_2\text{O}_7$.

Previous experimental research consistently reflected that the adsorption product with O_2 existence is AsO_4^{3-} , while different opinions existed regarding the adsorption structures. The study of Jadhav [12] found that the adsorption product obtained under 500 °C was mainly $\text{Ca}_3\text{As}_2\text{O}_8$ (JCPDS No.01-0933). Under 700 °C and 900 °C, the product was $\text{Ca}_2\text{As}_2\text{O}_7$ (JCPDS No.17-0444). When the temperature increased to 1000 °C, the reaction product was $\text{Ca}_3\text{As}_2\text{O}_8$ (JCPDS No.26-0295). Mahuli [41] (600 °C and 1000 °C) and Sterling [11] (800 °C) found that the adsorption product was $\text{Ca}_3\text{As}_2\text{O}_8$ (JCPDS No. 26-0295), while the sorbent used by Mahuli was $\text{Ca}(\text{OH})_2$. Li [13] found that the product obtained under 600 °C mainly belonged to $\text{Ca}_3\text{As}_2\text{O}_8$ crystal structure (JCPDS No. 01-0933), and another kind of $\text{Ca}_3\text{As}_2\text{O}_8$ crystal (JCPDS No. 73-1928) was identified for the products obtained under 800 °C and 1000 °C.

The role of temperature on adsorption product transformation is qualitatively described. The more detailed description of the product layer development is associated with many other factors, such as the concentration and flow rate of As_2O_3 and O_2 , and the quantity and granular size of CaO . The quantitative description of the adsorption process is still a very difficult challenge. Nevertheless, the DFT calculation findings revealed by this study could directly explain the experimental results obtained by previous researchers, which might provide some meaningful insight to understand the process of As_2O_3 adsorption on CaO .

4. Conclusions

The mechanisms of As_2O_3 adsorption on a CaO surface have been studied by using DFT calculation; conclusions are as follows:

- (1) Physisorption active sites are composed of superficial Ca atoms that interact with O of As_2O_3 . Chemisorption active sites are superficial O atoms that interact with As of As_2O_3 ;
- (2) The adsorption process can be described as follows: the isolated As_2O_3 molecule is firstly adsorbed on the CaO surface by physisorption, and then physisorbed As_2O_3 will transform to chemisorbed As_2O_3 . Due to thermal vibration, the chemisorbed As_2O_3 would overcome the energy barrier and transform to a more stable chemisorbed As_2O_3 state. The adsorption product is AsO_3^{3-} ;
- (3) The adsorption products of As_2O_3 under an O_2 -containing atmosphere are AsO_4^{3-} . The adsorption product's structure is influenced by the adsorption temperature. Under relatively low-temperature, the product is $\text{Ca}_3\text{As}_2\text{O}_8$; under relatively medium-temperature, the product is $\text{Ca}_3\text{As}_2\text{O}_7$; and under relatively high-temperature, the product is $\text{Ca}_3\text{As}_2\text{O}_8$.

The consistency between DFT calculation and the previous experiments proves high possibilities to design and optimized the CaO -based adsorbents by modifying O sites or other elements. Besides, other flue gases such as SO_2 or CO_2 can be involved in the following study to achieve materials design under real flue gas conditions. The optimized CaO -based adsorbents should be of high industrial value, could be applied in the injection of limestone into the furnace, CaO looping reactor, and dry desulfurization, etc.

Supplementary Materials: The following are available online at <http://www.mdpi.com/1996-1944/12/4/677/s1>. Table S1: Changes in physical and chemical properties of different surface size; Table S2: Changes in physical and chemical properties of different layers; Figure S1: Initial adsorbate structures; Figure S2: Paths and structures of

the physisorption and chemisorption reaction from chemisorption structure 1; Figure S3: PDOS of As₂O₃ and CaO surface during physisorption and chemisorption (a. PDOS of As₂O₃ molecule; and b. PDOS of CaO surface).

Author Contributions: Research Design, Y.F. and Y.Z.; Data collection, Y.F.; Data analysis, Y.F., Q.W., S.D., P.H. and D.L.; Figures and Tables, Q.W.; Manuscript draft, Y.F., Q.W., Y.Z. and S.D.; Manuscript revise, P.H. and D.L.

Funding: This work was financially supported by the National Natural Science Foundation of China No. 51776107.

Conflicts of Interest: The authors declare no conflict of interest.

References

1. Liu, R.; Yang, J.; Xiao, Y.; Liu, Z. Fate of Forms of arsenic in Yima coal during pyrolysis. *Energy Fuels* **2009**, *23*, 2013–2017. [CrossRef]
2. Clarke, L.B.; Sloss, L.L. *Trace Elements-Emissions from Coal Combustion and Gasification*; IEA Coal Research: London, UK, 1992; Volume 8, pp. 1822–1826.
3. Gao, J.; Yu, J.; Yang, L. Urinary arsenic metabolites of subjects exposed to elevated arsenic present in coal in Shaanxi province, China. *Int. J. Environ. Res. Public Health* **2011**, *8*, 1991–2008. [CrossRef] [PubMed]
4. Kapaj, S.; Peterson, H.; Liber, K.; Bhattacharya, P. Human health effects from chronic arsenic poisoning—A review. *J. Environ. Sci. Health Part A* **2006**, *41*, 2399–2428. [CrossRef] [PubMed]
5. 1990 Clean Air Act Amendment. Public Law; 1990. Available online: <https://www.gpo.gov/fdsys/pkg/USCODE-2013-title42/html/USCODE-2013-title42-chap85-subchapI-partA-sec7412.htm> (accessed on 11 February 2019).
6. Duan, J.; Tan, J.; Hao, J.; Chai, F. Size distribution, characteristics and sources of heavy metals in haze episod in Beijing. *J. Environ. Sci.* **2014**, *26*, 189–196. [CrossRef]
7. Pacyna, J.M.; Pacyna, E.G. An assessment of global and regional emissions of trace metals to the atmosphere from anthropogenic sources worldwide. *Environ. Rev.* **2001**, *9*, 269–298. [CrossRef]
8. Tian, H.; Liu, K.; Zhou, J.; Lu, L.; Hao, J.; Qiu, P.; Gao, J.; Zhu, C.; Wang, K.; Hua, S. Atmospheric Emission Inventory of Hazardous Trace Elements from China's Coal-Fired Power Plants Temporal Trends and Spatial Variation Characteristics. *Environ. Sci. Technol.* **2014**, *48*, 3575–3582. [CrossRef] [PubMed]
9. Mercury and air toxics Standards (MATS). Public Law; 2013. Available online: <https://www.epa.gov/mats> (accessed on 11 February 2019).
10. Helsen, L. Sampling technologies and air pollution control devices for gaseous and particulate arsenic: A review. *Environ. Pollut.* **2005**, *137*, 305–315. [CrossRef] [PubMed]
11. Sterling, R.O.; Helble, J.J. Reaction of arsenic vapor species with fly ash compounds: Kinetics and speciation of the reaction with calcium silicates. *Chemosphere* **2003**, *51*, 1111–1119. [CrossRef]
12. Jadhav, R.A.; Fan, L. Capture of gas-phase arsenic oxide by lime: Kinetic and mechanistic studies. *Environ. Sci. Technol.* **2001**, *35*, 794–799. [CrossRef] [PubMed]
13. Li, Y.; Tong, H.; Zhuo, Y.; Li, Y.; Xu, X. Simultaneous removal of SO₂ and trace As₂O₃ from flue gas: Mechanism, kinetics study, and effect of main gases on arsenic capture. *Environ. Sci. Technol.* **2007**, *41*, 2894–2900. [CrossRef] [PubMed]
14. Li, Y. *Experimental Study on Simultaneous Removal of Trace Selenium and Arsenic in Flue Gas Desulphurization within Medium Temperature Range*; Tsinghua University: Beijing, China, 2006.
15. López-Antón, M.A.; Díaz-Somoano, M.; Spears, D.A.; Martínez-Tarazona, M.R. Arsenic and selenium capture by fly ashes at low temperature. *Environ. Sci. Technol.* **2006**, *40*, 3947–3951. [CrossRef] [PubMed]
16. Shah, P.; Strezov, V.; Stevanov, C.; Nelson, P.F. Speciation of arsenic and selenium in coal combustion products. *Energy Fuels* **2007**, *21*, 506–512. [CrossRef]
17. Huggins, F.E.; Senior, C.L.; Chu, P.; Ladwig, K.; Huffman, G.P. Selenium and arsenic speciation in fly ash from full-scale coal-burning utility plants. *Environ. Sci. Technol.* **2007**, *41*, 3284–3289. [CrossRef] [PubMed]
18. Tian, C.; Gupta, R.; Zhao, Y.; Zhang, J. Release Behaviors of Arsenic in Fine Particles Generated from a Typical High-Arsenic Coal at a High Temperature. *Energy Fuels* **2016**, *30*, 6201–6209. [CrossRef]
19. Jialin, Y.; Jingjing, X.; Qinfang, Z.; Binwen, Z.; Baolin, W. First-principles studies on the structural and electronic properties of As clusters. *Materials* **2018**, *11*, 1596.
20. Li, Z.; Yangwen, W.; Jian, H.; Qiang, L.; Yongping, Y.; Laibao, Z. Mechanism of mercury adsorption and oxidation by oxygen over the CeO₂ (111) surface: A DFT study. *Materials* **2018**, *11*, 485.

21. Zhang, S.; Hu, X.; Lu, Q.; Zhang, J. Density functional theory study of arsenic and selenium adsorption on the CaO (001) surface. *Energy Fuels* **2011**, *25*, 2932–2938. [[CrossRef](#)]
22. Segall, M.D.; Lindan, P.J.; Probert, M.A.; Pickard, C.J.; Hasnip, P.J.; Clark, S.J.; Payne, M.C. First-principles simulation: Ideas, illustrations and the CASTEP code. *J. Phys. Condens. Matter* **2002**, *14*, 2717. [[CrossRef](#)]
23. Clark, S.J.; Segall, M.D.; Pickard, C.J.; Hasnip, P.J.; Probert, M.I.; Refson, K.; Payne, M.C. First principles methods using CASTEP. *Cryst. Mater.* **2005**, *220*, 567–570. [[CrossRef](#)]
24. Burke, K.; Ernzerhof, M.; Perdew, J.P. Generalized Gradient Approximation Made Simple. *Phys. Rev. Lett.* **1996**, *77*, 3865–3868.
25. Vanderbilt, D. Soft self-consistent pseudopotentials in a generalized eigenvalue formalism. *Phys. Rev. B Condens. Matter* **1990**, *41*, 7892. [[CrossRef](#)] [[PubMed](#)]
26. Von Barth, U.; Hedin, L. A local exchange-correlation potential for the spin polarized case. i. *J. Phys. C Solid State Phys.* **1972**, *5*, 1629. [[CrossRef](#)]
27. Press, W.H.; Teukolsky, S.A.; Vetterling, W.T.; Flannery, B.P. *Numerical Recipes in C.*; Cambridge University Press: Cambridge, UK, 1996; Volume 2.
28. Halgren, T.A.; Lipscomb, W.N. The synchronous-transit method for determining reaction pathways and locating molecular transition states. *Chem. Phys. Lett.* **1977**, *49*, 225–232. [[CrossRef](#)]
29. Henkelman, G.; Jónsson, H. Improved tangent estimate in the nudged elastic band method for finding minimum energy paths and saddle points. *J. Chem. Phys.* **2000**, *113*, 9978–9985. [[CrossRef](#)]
30. Monkhorst, H.J.; Pack, J.D. Special points for Brillouin-zone integrations. *Phys. Rev. B Condens. Matter* **1976**, *13*, 5188. [[CrossRef](#)]
31. Ghebouli, M.A.; Ghebouli, B.; Bouhemadou, A.; Fatmi, M.; Bouamama, K. Structural, electronic, optical and thermodynamic properties of $Sr_xCa_{1-x}O$, $Ba_xSr_{1-x}O$ and $Ba_xCa_{1-x}O$ alloys. *J. Alloys Compd.* **2011**, *509*, 1440–1447. [[CrossRef](#)]
32. Verbraeken, M.C.; Suard, E.; Irvine, J.T. Order and disorder in $Ca_2Nd_{0.90}H_{0.10}$ —A structural and thermal study. *J. Solid State Chem.* **2011**, *184*, 2088–2096. [[CrossRef](#)]
33. Da Hora, G.C.A.; Longo, R.L.; Da Silva, J.B.P. Calculations of structures and reaction energy profiles of As_2O_3 and As_4O_6 species by quantum chemical methods. *Int. J. Quantum Chem.* **2012**, *112*, 3320–3324. [[CrossRef](#)]
34. Liu, H.; Xiang, H.; Gong, X.G. First principles study of adsorption of O_2 on Al surface with hybrid functionals. *J. Chem. Phys.* **2011**, *135*, 214702. [[CrossRef](#)] [[PubMed](#)]
35. Fan, Y.; Yao, J.G.; Zhang, Z.; Sceats, M.; Zhuo, Y.; Li, L.; Maitland, G.C.; Fennell, P.S. Pressurized calcium looping in the presence of steam in a spout-fluidized-bed reactor with dft analysis. *Fuel Process. Technol.* **2018**, *169*, 24–41. [[CrossRef](#)]
36. Fan, Y.; Zhuo, Y.; Zhu, Z.; Du, W.; Li, L. Zerovalent selenium adsorption mechanisms on a CaO surface: DFT calculation and experimental study. *J. Phys. Chem. A* **2017**, *121*, 7385. [[CrossRef](#)] [[PubMed](#)]
37. Fan, Y.; Zhuo, Y.; Li, L. SeO_2 adsorption on a CaO surface: DFT and experimental study on the adsorption of multiple SeO_2 molecules. *Appl. Surf. Sci.* **2017**, *420*, 465–471. [[CrossRef](#)]
38. Sun, S.; Zhang, D.; Li, C.; Wang, Y.; Yang, Q. Density functional theory study of mercury adsorption and oxidation on CuO (111) surface. *Chem. Eng. J.* **2014**, *258*, 128–135. [[CrossRef](#)]
39. Xiang, W.; Liu, J.; Chang, M.; Zheng, C. The adsorption mechanism of elemental mercury on CuO (110) surface. *Chem. Eng. J.* **2012**, *200*, 91–96. [[CrossRef](#)]
40. Nørskov, J.K.; Studt, F.; Abild-Pedersen, F.; Bligaard, T. *Fundamental Concepts in Heterogeneous Catalysis*; John Wiley & Sons: Hoboken, NJ, USA, 2014.
41. Mahuli, S.; Agnihotri, R.; Chauk, S.; Ghosh-Dastidar, A.; Fan, L.-S. Mechanism of Arsenic Sorption by Hydrated Lime. *Environ. Sci. Technol* **1998**, *31*, 3226–3231. [[CrossRef](#)]

